Reprinted from February 1988, Volume 110, Journal of Offshore Mechanics and Arctic Engineering

Analysis and Prediction of Short-Term Ice Drift

M. G. McPhee
McPhee Research Company,
Yakima, Wash. 98908

Techniques for kinematic analysis and dynamic, "free-drift" ice modeling are described and applied to interpretation of ice-drift data from recent marginal ice zone (MIZ) experiments. Kinematic description is based on a complex demodulation algorithm that separates inertial and tidal components from lower frequency, "synoptic" drift. Complex demodulation produces the time series of phasors (complex numbers describing phase and amplitude of the oscillating components), useful for separating the physical processes active in the upper ocean/ice system. Free-drift ice motion modeling utilizes a similarity theory for planetary-boundary-layer dynamics that includes the effect of buoyancy, both from rapid melting at the ice/ocean interface, and/or from a pre-existing density gradient (pycnocline) within the boundary layer. Two examples are considered: one in which a band of ice in the Bering Sea drifted rapidly away from the rest of the pack when it encountered warm water at the ice edge; and a second in which drift in the Greenland Sea was apparently affected by both a shallow pycnocline and a period of rapid melt.

1 Introduction

Accurate prediction of short-term ice drift requires understanding of both the kinematics of local ice motion that has occurred in the time before the forecast, and of the physics of air-ice-sea interaction that will govern motion during the forecast period. The importance of the latter is self evident; the former is significant because the physical system often exhibits large oscillations at inertial or tidal frequencies. While these oscillations are not difficult to simulate (e.g., McPhee, 1980), any one who has tried to model them recognizes that the initial conditions, which a proper kinematic description can provide, have large impact on model solutions. One aim of this paper is to demonstrate a relatively simple technique for fitting randomly sampled ice position or velocity data to provide accurate kinematic descriptions.

In the physics of ice-drift modeling, the role of the oceanic boundary layer is often relegated to a single drag coefficient (perhaps with turning) which enters the ice momentum equation, and is used to parameterize the stress at the ice/ocean interface in terms of the square of the velocity difference between the ice and the undisturbed ocean. This approach masks a number of potentially important factors that enter into the actual boundary-layer problem, including variation of the drag and turning with surface Rossby number; variation in the surface roughness; stabilizing effects of surface melting or freezing; and density gradients in the underlying fluid. A second purpose of the paper is to show ways in which these effects can be incorporated into a reasonably compact generalization of the drag-coefficient problem, illustrated with examples from recent marginal ice zone experiments.

Contributed by the OMAE Division and presented at the 5th International Symposium and Exhibit on Offshore Mechanics and Arctic Engineering, Tokyo, Japan, April 13–22, 1986, of THE AMERICAN SOCIETY OF MECHANICAL ENGINEERS. Manuscript received by the OMAE Division, April 1, 1985; revised manuscript received August 3, 1987.

2 Kinematic Analysis of Ice Drift

Ice-drift trajectories often include circular or elliptical loops superimposed on a more-or-less steady translation. A rotary-spectral analysis of such motion typically shows spectral peaks near preferred inertial and tidal frequencies. Predominant tidal periods are diurnal and semi-diurnal. At high latitudes, inertial and semi-diurnal frequencies are difficult to resolve, especially with short records (a possible exception might be strong counterclockwise looping, which would indicate tidal forcing in the Northern Hemisphere), so in what follows no distinction is made. Usually, the velocity field must be synthesized from geographical position data, e.g., from satellite navigators or radar tracking, which are often irregularly sampled in time. Occasionally, ice velocity is available directly, for example, when a current meter suspended from drifting ice passes through water known to be nearly quiescent. Even then, a mathematical description of the field is needed for extrapolation. This section describes a complex demodulation procedure for fitting position data, which provides a mathematical function for the continuous velocity field. If velocity is sampled rather than position, the procedure is analogous, with one less coefficient required in the fitting. We assume that the trajectory can be described as a superposition of mean motion plus circular or elliptical oscillations at the inertial and diurnal frequencies over a time period comparable to the longest oscillating period; the method is an extension of one used by Perkins (1970) to analyze inertial waves in current meter records. The velocity is then

$$\hat{V}(t) = \hat{V}_m + \hat{S}_{cw}\, e^{-ift} + \hat{S}_{ccw}\, e^{ift} + \hat{D}_{cw}\, e^{-i\omega t} + \hat{D}_{ccw}\, e^{i\omega t} \quad (1)$$

where f is the angular frequency of the inertial/semi-diurnal oscillations with phase and amplitude described by the complex phasors (terminology borrowed from electronics, where, e.g., an alternating current is characterized by a complex constant containing amplitude and phase information), $\hat{S}_{cw}$

and $\hat{S}_{ccw}$. $\hat{D}_{cw}$, $\hat{D}_{ccw}$, and ω similarly describe the diurnal oscillation. Carets indicate complex quantities (i is the imaginary number, $i^2 = -1$); in the remainder of the paper, if a normally complex quantity is written without the caret, scalar magnitude is implied.

Integrating from initial position $\hat{X}_\phi$ with an arbitrary reference time, $t = 0$, we have

$$\hat{X} = \hat{X}_0 + \hat{V}_m t + (i/f)\{\hat{S}_{cw}(e^{-ift} - 1) + \hat{S}_{ccw}(1 - e^{ift})\} + (i/\omega)\{\hat{D}_{cw}(e^{-i\omega t} - 1) + \hat{D}_{ccw}(1 - e^{i\omega t})\} \quad (2)$$

The problem is to determine, in a least-mean-squares-error sense, the complex coefficients in (2), and reduces to solving the following system of linear equations using straightforward complex algebra:

$$\Phi = \Gamma^{-1} \cdot R$$

$$\Phi = (\hat{X}_0, \hat{V}_m, \hat{S}_{cw}, \hat{S}_{ccw}, \hat{D}_{cw}, \hat{D}_{ccw}) \quad (3)$$

where Γ is a symmetric, 6×6 matrix:

$$\begin{bmatrix} N & \sum t & \sum \hat{B}(f) & \sum \hat{B}(-f) & \sum \hat{B}(\omega) & \sum \hat{B}(-\omega) \\ \cdots & \sum t^2 & \sum t\hat{B}(f) & \sum t\hat{B}(-f) & \sum t\hat{B}(\omega) & \sum t\hat{B}(-\omega) \\ \cdots & \cdots & \sum \hat{B}(f)\hat{B}(f) & \sum \hat{B}(f)\hat{B}(-f) & \sum \hat{B}(f)\hat{B}(\omega) & \sum \hat{B}(f)\hat{B}(-\omega) \\ \cdots & & \cdots & \sum \hat{B}(-f)\hat{B}(-f) & \sum \hat{B}(-f)\hat{B}(\omega) & \sum \hat{B}(-f)\hat{B}(-\omega) \\ \cdots & & & \cdots & \sum \hat{B}(\omega)\hat{B}(\omega) & \sum \hat{B}(\omega)\hat{B}(-\omega) \\ \cdots & & & & \cdots & \sum \hat{B}(-\omega)\hat{B}(-\omega) \end{bmatrix}$$

$$R = \begin{vmatrix} \sum \hat{X} \\ \sum t\hat{X} \\ \sum \hat{B}(f)\hat{X} \\ \sum \hat{B}(-f)\hat{X} \\ \sum \hat{B}(\omega)\hat{X} \\ \sum \hat{B}(-\omega)\hat{X} \end{vmatrix}$$

where we have used the following notation:

$$\hat{B}(\alpha) = (i/\alpha)(e^{-i\alpha t} - 1)$$

$$\sum \alpha = \sum_{i=1}^{N} \alpha_i$$

N being the number of samples in the fitting period. The matrix equation is solved by Gaussian elimination.

To demonstrate the technique, we apply it to navigation data from the M/V POLARQUEEN during its MIZEX 84 drift in the Greenland Sea. For a 40-day period in the summer of 1984, the ship was moored to floes, initially located 50–100 km inside the ice edge, and allowed to drift. The drift occurred in two phases. The first started at about day 159.5 (i.e., noon GMT on June 7, 1984), and was terminated early on day 168, after persistent northerly winds forced the floe into the immediate ice-edge region, where it was broken by ocean swell. The ship and its surrounding instrument array were then redeployed about 60 km northwest, and the ship remained moored to one floe for 30 days, from 170 to 200.

Figure 1 shows each fix from the onboard, dual channel satellite navigator considered acceptable by the navigator's algorithm for determining dead-reckoning ship position. These fixes were randomly spaced in time, usually with 35 to 40 good fixes per day available. Typical accuracy for one fix is 50–100 m.

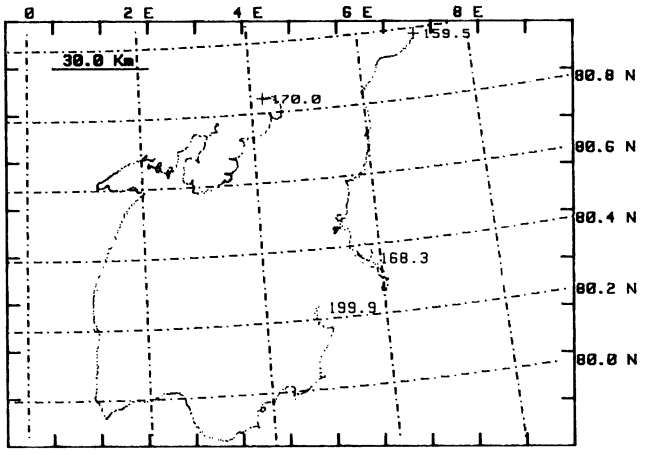

Fig. 1 All satellite navigation fixes for the M/V POLARQUEEN during the two passive drifts of MIZEX 84. Numbers at end of segments are calendar days of 1984, e.g., 159.5 = 1200 GMT on June 7, 1984.

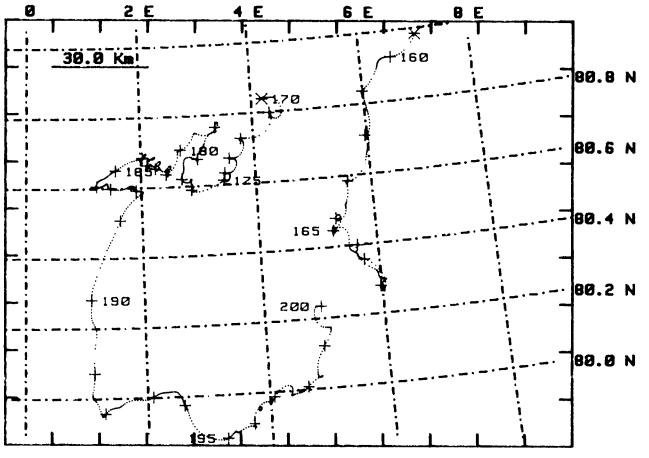

Fig. 2 Fitted trajectories with position plotted hourly. Pluses indicate 0000 GMT of each day.

Time series of the six complex coefficients in (2) were calculated every 3 hr from a 24-hr interval centered at the fit time. Values used for inertial (semi-diurnal) and diurnal periods were 12.2 and 24 hr, respectively. The resulting file of fit parameters are saved, and may subsequently be used to determine position or velocity at any time. Figure 2 shows the fitted drift track with positions plotted every hour, and time marks at 0000 GMT of each day.

Kinematics of the ice velocity field is shown in Fig. 3. The topmost row of arrows, V_m, is essentially the 24-hr, low-pass filtered ice velocity. The remaining rows are phasors representing amplitude and phase of clockwise and counterclockwise oscillations at the semi-diurnal (inertial) frequency, denoted S, and diurnal frequency, D. A train of phasors of similar magnitude and alignment indicates a steady (and predictable) inertial or tidal oscillation.

The events starting on about day 174 demonstrate the interplay between mean velocity and the phasors. From Fig. 3, we see that the mean velocity rotates full circle over the following week. Figure 4 is a blowup from Fig. 2, including all the actual fixes (dots) in the time period 174 to 184. The mean drift starts out to the southwest from near rest, veers around to northeast, then rapidly rotates to southwest on 179, and peters out by 181. The slowly decaying train of semi-diurnal ($\hat{S}_{cw}$) phasors starting at about 179 may be interpreted as inertial response to rapid changes in the wind. Note that the inertial oscillation remains coherent and energetic for several days after the mean drift dies down. During the early part of the inertial event, the tidal ($\hat{D}_{cw}$, $\hat{D}_{ccw}$) phasors are

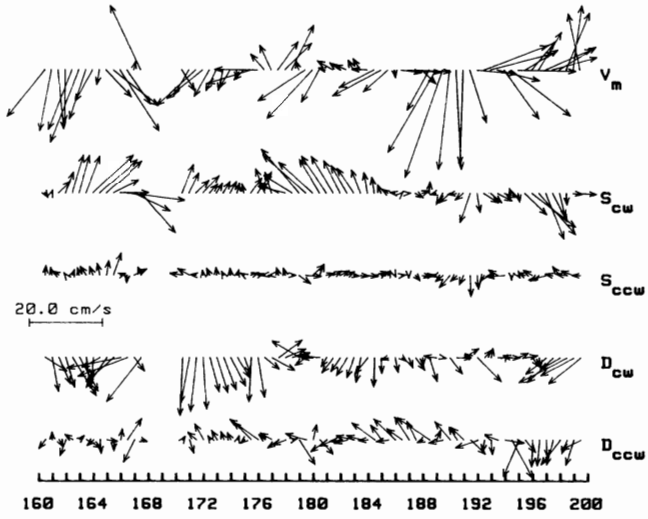

Fig. 3 Time series of filtered drift vector ($\hat{V}_m$), and oscillation phasors as described in the text for the time period 160 to 200 of 1984, plotted every 12 hr. Up is north.

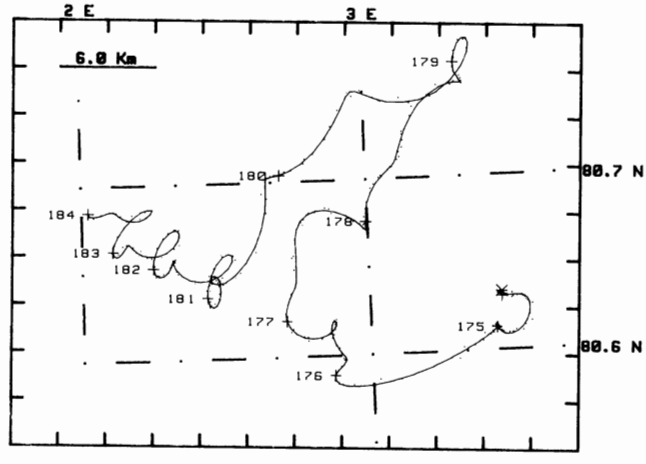

Fig. 4 POLARQUEEN trajectory segment, 174 to 184, showing each navigation fix (dots) and fitted trajectory (solid). Note the intricate loops following 181.

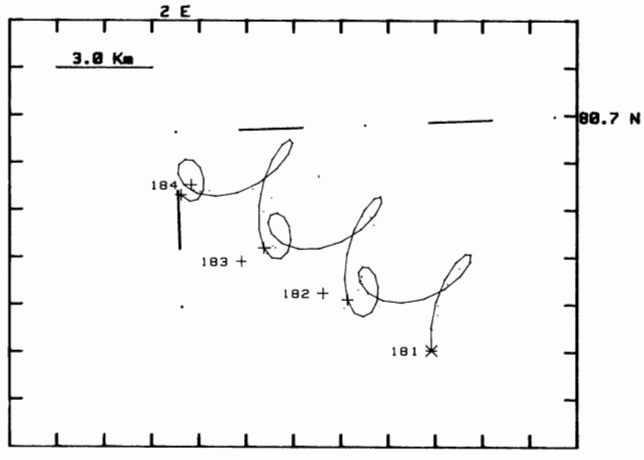

Fig. 5 Solid line is trajectory calculated by integrating sum of constant mean current and inertial and tidal components calculated from phasors for time 181.0. Dots are hourly values of fitted data.

mixed and small, and so the trajectory from 179 to say, 180.5, takes the classic scalloped appearance of circular inertial motion superimposed on mean drift. After 180, a small, but persistent tidal signal distorts the inertial oscillations.

To illustrate the utility of the phasors, an extrapolation of a constant phasor field superimposed on a small, steady drift is shown in Fig. 5. The dots are hourly values of position taken from the file of fitted coefficients for the period 181 to 184. Recall that the fit parameters are generated every 3 hr, and the fitted trajectory coincides closely with navigation fixes as shown by Fig. 4. The solid curve is the integral of velocity obtained by adding a small mean drift to oscillations calculated with constant coefficients fitted for time 181.0 only; i.e.,

$$\hat{X}_{t'} = \hat{X}_{181} + \int_{t=181}^{t'} \hat{V}(t)\, dt \tag{4}$$

where $\hat{V}(t)$ is given by (1). $\hat{V}_m$ is (−3.2, 2.0) cm/s; $\hat{X}_{181}$ is position at time 181.0 and the phasors are constant, calculated from data in a 24-hr window centered at time 181.0. This is not a forecast, since we chose the constant mean current to coincide with displacement from 181 to 184, i.e., a straight line from 181 to 184. Rather, it demonstrates that if the underlying mean drift is known or can be estimated, kinematic information obtained by fitting over a limited period prior to the forecast may be used to predict with some success the rather intricate looping motions seen in the actual trajectory. If a model for simulating the oscillatory behavior exists, then the phasors may be used for specifying the initial velocity field. Prediction of the underlying velocity field is the topic of Section 3.

3 The Free Drift of Sea Ice

In the previous section we saw that ice motion can often be successfully decomposed into oscillating inertial and tidal components plus an underlying "mean" drift. This underlying velocity is often correlated closely with surface wind, especially in situations where the ice is diverging, or where it is not compact or strong enough to support mean internal stress gradient. The free-drift response of pack ice (i.e., when the balance of forces is dominated by air stress, water stress, and Coriolis force) in the central Arctic Basin, and its implications for ocean boundary layer structure are discussed in McPhee (1979) and McPhee (1982). A simple similarity theory that incorporated the results of free-drift studies into a generalized solution for the neutral and stably stratified boundary layer is described by McPhee (1981), and this theory was subsequently extended to include the effects of a shallow pycnocline on boundary-layer velocity structure (McPhee, 1983).

In this section, the extended theory is demonstrated by two examples from the MIZ: one in which the ice drifted into warm water and melted rapidly; and a second in which drift was affected first by a shallow pycnocline, and later by rapid melt. In both cases the modeled ice drift is noticeably different from previous free-drift simulations, and apparently closer to the observed drift.

Theory. In complex notation, the free-drift momentum equation is

$$\hat{\tau}_a - \hat{\tau}_w = i\rho_i h_i \hat{U}_o \tag{5}$$

where $\hat{\tau}_a$ is surface wind stress; $\hat{\tau}_w$ is stress at the ice/ocean interface; ρ_i and h_i are mean ice density and thickness; and $\hat{U}_o$ is ice velocity relative to geostrophic flow at the surface (i.e., the flow proportional to surface tilt). We define the complex (vector) friction velocity as

$$\rho_o u_*\hat{u}_* = \hat{\tau}_w$$

We also define a nondimensional surface velocity relative to flow at the base of the frictional boundary layer, in terms of the relative ice velocity.

$$\hat{u}_o = \eta_* \frac{\hat{U}_o}{\hat{u}_*}$$

where η_* is a scaling factor that depends on buoyancy. Rearranging (5), we have

$$\hat{u}_* = \frac{\hat{\tau}_a}{\rho_a u_* + \dfrac{i\rho_i h_i \hat{u}_o}{\eta_*}} \tag{6}$$

The equation is implicit, because scalar friction speed, u_*, appears on the right side, both directly and indirectly through $\hat{u}_o$ and η_*. From McPhee (1981), the nondimensional surface velocity is given by

$$\hat{u}_o = \hat{u}_E - \frac{\eta_*}{k}\left\{\ln\frac{|\zeta_o|}{\xi_N} + (\hat{\delta} - a)\xi_N + \frac{a}{2}\hat{\delta}\xi_N^2\right\} \tag{7}$$

$$\hat{\delta} = \left(\frac{i}{k\xi_N}\right)^{1/2}$$

ξ_N is a constant, equal to 0.052; ζ_o is the nondimensional surface to roughness

$$\zeta_o = \frac{fz_o}{\eta_* u_*}$$

and

$$a = \frac{1 - \eta_*}{\eta_* \xi_N}$$

$\hat{u}_E$ is the nondimensional velocity at the top of the "free-turbulence" (Ekman) layer.

Solution of (6) involves an iterative operation in which $\hat{u}_o$ is first calculated, assuming that

$$\rho_o u_* \hat{u}_* = \hat{\tau}_a$$

The new value of $\hat{u}_o$ is used in (6) to calculate $\hat{u}_*$, and this is repeated until the change in u_* from one iteration to the next falls below a specified tolerance. In practice, the convergence occurs rapidly.

The present theory departs from previous work in the way that buoyancy effects enter, either through direct input at the surface (from rapid melt) or from a shallow pycnocline. When there is no surface buoyancy flux, $\eta_* = 1$. If, in addition, the mixed-layer depth is greater than the rotational boundary-layer depth (about $0.4\, u_*/f$), u_E is given by

$$\hat{u}_E = -i\hat{\delta}e^{-\hat{\delta}\xi_N} \tag{8}$$

Under these conditions, (7) reduces to a Rossby-similarity drag law, appropriate to high Arctic conditions as determined from the AIDJEX experiments a decade ago (see McPhee, 1982)

$$\hat{u}_o = \frac{1}{k}\{(\ln Ro_* - A) - i \cdot B\}; \qquad \begin{cases} |z_{pyc}| \text{ large} \\ \eta_* = 1 \end{cases}$$

$$Ro_* = u_*/(fz_o) \tag{9}$$

For $\xi_N = 0.052$, $A = 2.12$ and $B = 2.11$.

Surface buoyancy flux enters the ice drift model through the scaling factor η_*, which depends on u_* and melt rate. For the case where ice drifts into warm water, what we seek is a way of calculating η_* from the salinity and temperature characteristics of the new mixed layer into which the ice is advected. In a recent note (McPhee, 1985), I derived an approximation for η_* given by

$$\eta_* = \left\{1 + a_1 \cdot \frac{w}{u_*^2}(S_o - S_i)\right\}^{-1/2}$$

where $a_1 = 5.6$ m s^{-1} (‰)$^{-1}$, S_o is water salinity at the ice interface, S_i is ice salinity, and w is melt rate scaled by the ratio of ice density to water density. I also showed that the "nondimensional" melt rate is

$$\frac{w}{u_*} = \frac{T_{ff} - T_o}{Q_L \cdot \Lambda}$$

where T_{ff} is the temperature of the far field, T_o is the interfacial water temperature, and Q_L is the kinematic latent heat for sea ice, about 60°C. The nondimensional temperature change across the boundary layer is given by

$$\Lambda = \frac{1}{k}\ln\frac{u_*\xi_N}{fz_{oT}} + \frac{1}{2\xi_N\eta_*}$$

where z_{oT} is surface temperature roughness. The final equation relates interfacial salinity to far-field temperature and salinity, after elimination of the interfacial temperature using the freezing line relationship

$$\frac{S_o}{S_{ff}} = \frac{Q_L - \left(\dfrac{S_o - S_i}{S_{ff}}\right) \cdot T_{ff}}{Q_L + m(S_o - S_i)}$$

where $m = 0.06$°C (‰)$^{-1}$. Given u_*, T_{ff}, S_{ff}, and S_i, the equation for η_* is solved iteratively. In the solution for ice velocity, this becomes one more step in the iteration process for determining the interfacial stress.

Whether or not surface buoyancy flux is present, the drag (especially the angle between surface velocity and stress) is affected by the presence of density gradients near the surface. When the mixed-layer depth is less than the rotational scale, an implicit, algebraic equation for $\hat{u}_E$ is solved, requiring specification of both mixed-layer depth, z_{pyc}, and the Brunt-Väisälä frequency in the upper part of the underlying pycnocline; details are given in the Appendix.

Bering Sea Example. A dramatic example of buoyancy effect on ice drift comes from data gathered at the ice edge in the Bering Sea, described by Martin, Kauffman, and Parkinson (1983). In the experiment, two buoys were positioned near the ice edge, then tracked by radar from a nearby ship for about a day and a half. During this time, a band of ice containing the buoys steadily diverged from the main ice pack, while melting rapidly in the above-freezing water initially seaward of the marginal ice zone. Martin et al., invoked wave radiation pressure on the ice band to explain the observed divergence; however, a number of other possible mechanisms have been suggested, including the similarity theory described in this section. The essential idea in the similarity theory is that turbulent heat flux causes rapid ice melt, which introduces enough fresh melt water at the surface to significantly stabilize the boundary layer. Momentum is trapped in a thinner layer than it would be otherwise, and so the surface velocity is greater for the same surface stress. The situation is described in detail in McPhee (1983a).

For the Bering Sea example, the total displacement (after removing tidal and inertial motions) was modeled by integrating hourly solutions of the ice velocity calculated using wind measured at the nearby research vessel. Figure 6(*a*)

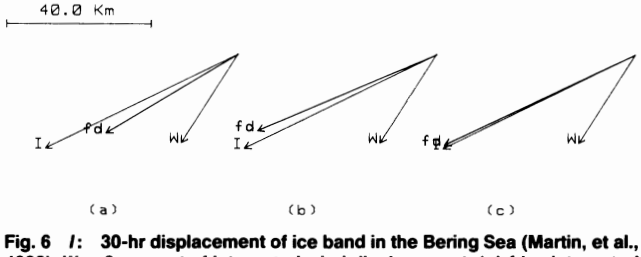

Fig. 6 *I*: 30-hr displacement of ice band in the Bering Sea (Martin, et al., 1983); *W*: 2 percent of integrated wind displacement. (*a*) *fd*: integrated displacement of free-drift velocity calculated hourly, with no melting; (*b*) same as (*a*) except far-field temperature rises from freezing to 0.5°C in the first 24 hr; (c) same as (*b*) except surface roughness, z_o, falls from 0.05 m to 0.01 m in the first 24 hr.

shows a comparison of the ice drift (I), wind displacement (scaled by 50), and integrated model displacement (fd), calculated assuming that water remains at its freezing point, so that there is no melting. For this calculation, wind stress is

$$\hat{\tau}_a = \rho_a C_{10} W \hat{W}$$

where W is the near-surface wind, and $c_{10} = 0.0027$. Other parameters are: $h_i = 2$ m, $z_o = 0.05$ m. The modeled drift is slower with less deflection angle than observed.

In Fig. 6(b), identical parameters were used except for water temperature, which increases from freezing at the start of the simulation to 0.5°C after 24 hr. This is approximately the sea-surface temperature structure observed from the research vessel drifting just ahead of the band (see Fig. 12 of Martin et al., 1983). Temperature roughness, z_{oT}, was set equal to 3×10^{-5} m. (Temperature roughness is the integration constant for the logarithmic temperature profile in the surface layer, thought to be smaller than momentum roughness, especially for rough surfaces.)

Finally, Fig. 6(c) demonstrates another possible effect of rapid melting. Here, the simulation is identical to 6(b) except that in addition to boundary-layer stabilization, melting decreases the surface (momentum) roughness, z_o, from 5 cm to 1 cm in 24 hr. The underside of ablated ice often appears much smoother than unmelted ice, and the assumption is that this manifests itself as decrease in surface roughness. The simulation is obviously very close to the observed motion, and provides a quantitatively realistic explanation for the divergence, since the leading band would leave cooler water behind. Ice following would tend to drift as in Fig. 6(a), as the water cools toward the freezing point.

Greenland Sea Example. The free-drift simulation is next applied to a 20-day segment of the drift of M/V POLARQUEEN, kinematics of which was discussed in Section 2. Wind was measured at a mast deployed on the ice floe near the ship, and for the simulations, the wind record was filtered with a 12-hr smoothing analogous to that used for ice motion.

A value of 0.0027 is used for the wind drag coefficient, based on previous ice studies in the central Arctic (McPhee, 1979). The mixed-layer depth was less than 15 m for much of the period, but deepened past the 15-m level for about a day during the strong wind event centered on about day 190. For the demonstration here, 15 m is used for the mean mixed layer depth. Stratification in the pycnocline immediately below the mixed layer is characterized by the buoyancy frequency, $N = 0.02$ s^{-1}. Preliminary analysis of turbulent stress and mean flow measured by the author in the underice boundary layer on days 189–190 indicates a surface roughness value, $z_o = 0.042$ m. Temperature of the mixed layer is taken from near continuous measurements at 7 m below the ice. Using these inputs, assuming average ice thickness to be 2 m, the similarity equations described above were solved for free-drift ice velocity every 12 hours and compared with the observed (filtered) drift. Figure 7 shows vector plots of the wind (scaled by 50 relative to the ice drift); the observed ice velocity after removing inertial and tidal motions; and, finally, the free-drift model, for a 20-day period encompassing two major wind events. Clearly, wind is the major forcing element in mean motion during this time.

Figures 8 and 9 demonstrate both aspects of buoyancy effect on ice drift. We consider the period of rapid southward drift that occurred from 189.0 to 192.0, shown as the smoothed ice trajectory (+ symbols with time marks) in Fig. 8. The other two trajectories are models: one which includes both the pycnocline and mixed-layer temperature effects (referred to a Model A, marked with crosses); the other model (Model B, circles) is the straight Rossby similarity drag given by (9)—essentially the drift response expected of ice in the central Arctic where buoyancy effects are small.

Figure 9 shows water temperature at 5 levels measured from the ice undersurface. During the first part of the period, water temperature is within a few tenths of a degree of freezing, and the main difference in the modeled trajectories comes from the 15-m pycnocline, which increases deflection in the boundary-layer mean current. Note that the total displacement in both observed and Model A trajectories on the first day is somewhat less than for Model B. Over the next

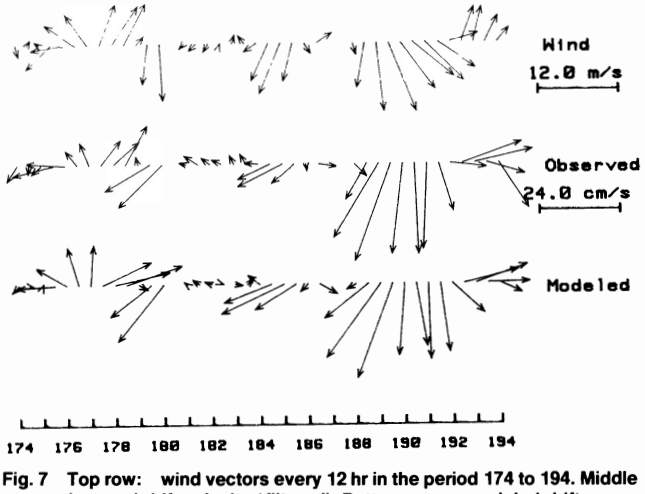

Fig. 7 Top row: wind vectors every 12 hr in the period 174 to 194. Middle row: observed drift velocity (filtered). Bottom row: modeled drift.

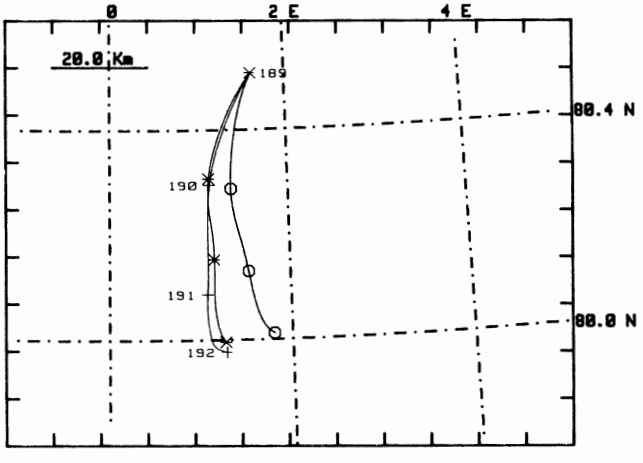

Fig. 8 3-day ice trajectory starting at 189.0. Pluses: observed; crosses: Model A, including 15-m pycnocline, and 7-m temperature; circles: Model B, assuming no buoyancy effects.

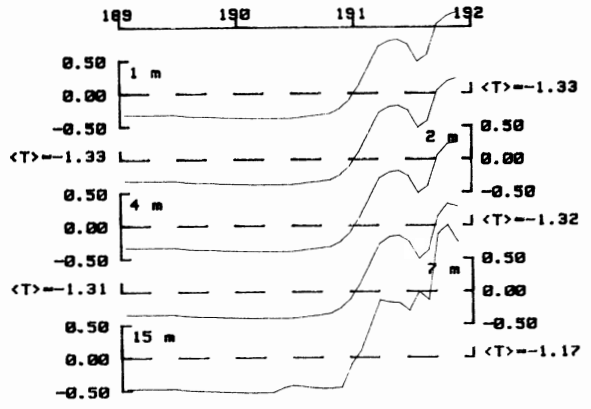

Fig. 9 Temperature in °C at 5 levels, drawn as deviation from mean. Time period is day 189 to 192 (July 7 to July 10) 1984. Numbers next to each axis are mean temperature during period shown.

two days, this trend reverses, with the total displacement from 190 to 192 considerably larger for observed and Model A than for Model B. In addition, there is more deflection to the west. In Model A, the acceleration and enhanced turning are clearly linked to the abrupt temperature front crossed later on day 190.

Despite the fact that observed and modeled displacement over the three days is remarkably similar, examination of Fig. 7 shows that the ice accelerated before we crossed the temperature front locally. Part of this is due to the smoothing performed on the displacement field to obtain "observed" mean velocity, but current meter records also showed that the ice acceleration preceded the temperature rise. A plausible cause is horizontal divergence in the ice and near-surface currents in the first few kilometers south of our local observations. Note that this case differs from the Bering Sea example in that the ice edge was several tens of kilometers away. To model this phenomenon more precisely would require a great deal more complexity; nevertheless, this example nicely demonstrates how both rapid melting and the presence of a seasonal pycnocline from accumulated melt can alter ice drift response.

4 Summary

In this paper, we have extended previous treatments of the free drift of sea ice to include a more sophisticated kinematic analysis technique for separating inertial and tidal motion from net drift, and we have outlined a relatively simple theory for wind-driven upper ocean currents that can be used to model phenomena seen in the complex environment near the ice edge. The kinematic analysis allows us to better determine what it is that we wish to model (for example, one might use the inertial phasors as initial conditions in a simulation of inertial oscillations that would be separate from the mean wind-drift response); and the free-drift model embodies a number of turbulence principles that have proved useful in other contexts.

The examples and analysis suggest a warning for operators concerned about ice encroachment. A sizable body of ice (one large enough to affect the oceanic boundary layer over a large area) drifting into relatively warm water may move considerably faster than it would in freezing water, especially under high wind conditions. However, the underlying cause of enhanced drift is rapid ablation, so that any threat may literally melt away.

The main thrust of the work is that while upper-ocean processes cannot be ignored in ice-drift modeling, neither do they necessarily require extensive and costly numerical models. The routines used in this work are all short and fast, and can be incorporated into ice-drift prediction schemes almost as easily as the conventional quadratic drag laws.

Acknowledgment

Wind data from M/V POLARQUEEN were supplied by K. Davidson and P. Guest of the Naval Postgraduate School. Data from the Bering Sea experiment were supplied by S. Martin of the University of Washington. G. Mellor of Princeton University supplied numerous pointers and much insight. Funding was provided by the Office of Naval Research under Contract N00014-84-C-0028. Their help is most gratefully acknowledged.

References

Martin, S., Kauffman, P., and Parkinson, C., 1983, "The Movement and Decay of Ice Edge Bands in the Winter Bering Sea," *Journal of Geophysical Research*, Vol. 88, pp. 2803–2812.

McPhee, M. G., 1979, "The Effect of the Oceanic Boundary Layer on the Mean Drift of Pack Ice: Application of a Simple Model," *Journal of Physical Oceanography*, Vol. 9, pp. 388–340.

McPhee, M. G., 1980, "A Study of Oceanic Boundary-Layer Characteristics Including Inertial Oscillation at Three Drifting Stations in the Arctic Ocean," *Journal of Physical Oceanography*, Vol. 10, pp. 870–884.

McPhee, M. G., 1981, "An Analytic Similarity Theory for the Planetary Boundary Layer Stabilized by Surface Buoyancy," *Boundary-Layer Meteorology*, Vol. 21, pp. 325–340.

McPhee, M. G., 1982, "Sea Ice Drag Laws and Simple Boundary Layer Concepts, Including Application to Rapid Melting," CRREL Report 82-4, U.S. Army Cold Regions Research and Engineering Laboratory, Hanover, N.H.

McPhee, M. G., 1983, "An Analytic Approach to Modelling Turbulent Exchange in the Upper Ocean," *Ocean Modelling*, Vol. 52, pp. 6–8.

McPhee, M. G., 1983a, "Turbulent Heat and Momentum Transfer in the Oceanic Boundary Layer Under Melting Pack Ice," *Journal of Geophysical Research*, Vol. 88, pp. 2813–2818.

McPhee, M. G., 1985, "A Note on Estimating Melt Rate in the MIZ," *MIZEX Bulletin*, Special Report Series, U.S. Army Cold Regions Research and Engineering Laboratory, Hanover, N.H.

Perkins, H., 1970, "Inertial oscillations in the Mediterranean," PhD thesis, MIT, Woods Hole.

APPENDIX

A density gradient away from the immediate ice/ocean interface is treated in the similarity theory described in Section 3 by solving an implicit, analytic equation for the stress at the mixed-layer/pycnocline derived as follows:

The nondimensional stress equation is

$$i\hat{T}/K_{\bullet} = \frac{\partial^2 \hat{T}}{\partial \zeta^2} \tag{10}$$

where $\hat{T}$ is nondimensional, turbulent stress

$$\hat{T} = \hat{\tau}/(\rho_o u_{\bullet} \hat{u}_{\bullet})$$

$K_{\bullet}$ is the nondimensional eddy viscosity

$$K_{\bullet} = fK_m/(u_{\bullet}^2 \eta_{\bullet}^2)$$

and the nondimensional vertical coordinate is

$$\zeta = fz/(u_{\bullet}\eta_{\bullet})$$

In the mixed layer, the solution of (10), and $-i$ times its derivative, which is velocity, are given by

$$\hat{T}(\zeta) = 2\hat{A} \cdot \sinh(\hat{\delta}\zeta) + e^{-\hat{\delta}\zeta}; \qquad 0 > \zeta \geq \zeta_p \tag{11}$$

$$\hat{u}(\zeta) = -i\hat{\delta}\{2\hat{A} \cdot \cosh(\hat{\delta}\zeta) - e^{-\hat{\delta}\zeta}\}; \qquad 0 > \zeta \geq \zeta_p \tag{12}$$

The eddy viscosity in the mixed layer is $K_{\bullet m} = k\xi_N$

$$\hat{\delta} = (i/K_{\bullet m})^{1/2}$$

In the lower layer (pycnocline), the solutions are the standard Ekman solutions scaled by the turbulent stress at the pycnocline, $\hat{T}_p$

$$\hat{T}(\zeta) = \hat{T}_p e^{\hat{\gamma}(\zeta - \zeta_p)}; \qquad \zeta < \zeta_p$$

$$\hat{u}(\zeta) = -i\hat{\gamma}\hat{T}_p e^{\hat{\gamma}(\zeta - \zeta_p)}; \qquad \zeta < \zeta_p$$

$$\hat{\gamma} = (i/K_{\bullet p})^{1/2}$$

where $K_{\bullet p}$ is the eddy viscosity in the upper part of the pycnocline.

By matching stress and velocity at the nondimensional pycnocline level, ζ_p, $\hat{A}$ is eliminated according to

$$\hat{A} = \frac{(\hat{\gamma} + \hat{\delta})e^{-\hat{\delta}\zeta_p}}{2 \cdot \{\hat{\delta}\cosh(\hat{\delta}\zeta_p) - \hat{\gamma}\sinh(\hat{\delta}\zeta_p)\}} \tag{13}$$

The problem is to close the equations by finding an expression for $K_{\bullet p}$. Define a friction velocity in the pycnocline by

$$u_{\bullet p}\hat{u}_{\bullet p} = \hat{T}_p u_{\bullet}\hat{u}_{\bullet}$$

and working by analogy with the original similarity theory, we assume that stratification in the pycnocline is always

sufficient to force turbulence to scale with the local Obukhov length; thus

$$K_p = ku_{*p}\mathrm{R_c L_p} \tag{14}$$

where

$$L_p = \frac{\rho_o u_{*p}^3}{kg \langle \rho' w' \rangle_p}$$

By Reynolds analogy, the eddy diffusivity for turbulent flux of any scalar quantity is proportional to eddy viscosity, so the buoyancy flux may be written in terms of mean quantities,

$$\frac{g}{\rho_o} \langle \rho' w' \rangle_p = -\frac{g}{\rho_o} \alpha K_p \left.\frac{\partial \rho}{\partial z}\right|_p = -\alpha N^2 K_p$$

where N is the Brunt-Väisälä frequency in the upper pycnocline. Substituting this into (14) and nondimensionalizing, we have

$$K_{*p} = fK_p/(u_* \eta_*)^2 = \sqrt{R_c/\alpha}\, \frac{f}{N} \cdot \frac{T_p}{\eta_*^2} \tag{15}$$

The interfacial stress magnitude, T_p, is still unknown; however, substitution of the expression for K_{*p} (15) into (13), which is in turn substituted into (11) evaluated at $\zeta = \zeta_p$ provides an implicit equation for the stress at the pycnocline, which is solved by iteration. The expression for $\hat{u}_E$ used in (7) to obtain surface velocity is found by evaluating (12) at $\zeta = -|\xi_N|$, once $\hat{T}_p$ is known.